


Surface Coating Enabling Sulfide Solid Electrolytes with Excellent Air Stability and Lithium Compatibility


Min Luo, Changhong Wang, Yi Duan, Xuyang Zhao, Jiantao Wang* , and Xueliang Sun*

All-solid-state lithium metal batteries (ASSLMBs) featuring sulfide solid electrolytes (SEs) are recognized as the most promising next-generation energy storage technology because of their exceptional safety and much-improved energy density. However, lithium dendrite growth in sulfide SEs and their poor air stability have posed significant obstacles to the advancement of sulfide-based ASSLMBs. Here, a thin layer (approximately 5 nm) of $g\text{-C}_3\text{N}_4$ is coated on the surface of a sulfide SE ($\text{Li}_6\text{PS}_5\text{Cl}$), which not only lowers the electronic conductivity of $\text{Li}_6\text{PS}_5\text{Cl}$ but also achieves remarkable interface stability by facilitating the in situ formation of ion-conductive Li_3N at the $\text{Li}/\text{Li}_6\text{PS}_5\text{Cl}$ interface. Additionally, the $g\text{-C}_3\text{N}_4$ coating on the surface can substantially reduce the formation of H_2S when $\text{Li}_6\text{PS}_5\text{Cl}$ is exposed to humid air. As a result, Li-Li symmetrical cells using $g\text{-C}_3\text{N}_4$ -coated $\text{Li}_6\text{PS}_5\text{Cl}$ stably cycle for 1000 h with a current density of 0.2 mA cm^{-2} . ASSLMBs paired with LiNbO_3 -coated $\text{LiNi}_{0.6}\text{Mn}_{0.2}\text{Co}_{0.2}\text{O}_2$ exhibit a capacity of 132.8 mAh g^{-1} at 0.1 C and a high-capacity retention of 99.1% after 200 cycles. Furthermore, $g\text{-C}_3\text{N}_4$ -coated $\text{Li}_6\text{PS}_5\text{Cl}$ effectively mitigates the self-discharge behavior observed in ASSLMBs. This surface-coating approach for sulfide solid electrolytes opens the door to the practical implementation of sulfide-based ASSLMBs.

1. Introduction

The demand for high-performance, long-lasting energy storage devices has intensified with the rapid growth of renewable energy sources, portable electronics, and electric vehicles. To meet this demand, lithium-ion batteries (LIBs) have become the dominant energy storage technology due to their high energy density, long cycle life, and excellent charge/discharge efficiency.^[1,2] However, the widespread application of conventional liquid electrolyte-based LIBs is hindered by safety concerns, limited energy density, and environmental issues.^[3,4] To

Dr. M. Luo, Dr. Y. Duan, X. Zhao, Prof. J. Wang
National Power Battery Innovation Center, GRINM Group Corporation Limited, Beijing 100088, China
China Automotive Battery Research Institute Co., Ltd., Beijing 100088, China
General Research Institute for Nonferrous Metals, Beijing 100088, China
E-mail: wangjt@glabat.com
Dr. C. Wang, Prof. X. Sun
Eastern Institute for Advanced Study, Eastern Institute of Technology, Ningbo 315200, China
E-mail: xsun@eitech.edu.cn

 The ORCID identification number(s) for the author(s) of this article can be found under <https://doi.org/10.1002/eem2.12753>.

DOI: 10.1002/eem2.12753

address these challenges, there has been an increasing interest in all-solid-state lithium metal batteries (ASSLMBs), which promise enhanced safety, wider operating temperature ranges, and the potential for higher energy densities.^[5–7] To enable ASSLMBs, numerous solid electrolytes (SEs) based on various anion chemistry have been developed, such as sulfides, oxides, halides, oxyhalides, and solid polymers.^[8–12] Among these choices, sulfide SEs demonstrate the highest ionic conductivity (e.g., 32 mS cm^{-1}) at room temperature.^[13] Therefore, sulfide-based all-solid-state batteries have demonstrated high power density, ultra-long cycling life, and outstanding low-temperature capacity retention.^[14,15] Despite the impressive electrochemical performance of sulfide-based all-solid-state batteries, several challenges have impeded their commercialization, especially the poor air stability of sulfide SEs and lithium dendrite growth.^[16–18] The former brings the release of harmful H_2S , which increases the manufacturing cost and environmental concerns. The latter leads to short-circuit and thermal runaway, which pose

a major safety concern. The formation of lithium dendrites is primarily attributed to uneven lithium deposition and the presence of defects in sulfide SEs, causing high localized electric field concentration.^[6,7]

Extensive studies have been conducted to address the aforementioned issues. Representative strategies, such as H_2S adsorbents, element doping, and surface engineering, have been employed to enhance the air stability of sulfide SEs. The physically blend of ionic insulating additives (Bi_2O_3 ,^[19] FeS ,^[20] ZSM-5 zeolite^[21]) with sulfide SEs can adsorb or decompose H_2S gas. However, this process adversely affects ionic conductivity and does not offer significant enhancement for the air stability of sulfide SEs. Based on the soft hard acid base theory, oxygen (O) was employed instead of sulfur (S)^[22,23] or a soft acid instead of phosphorous (P)^[24,25] to impede the hydrolysis reaction. Furthermore, a water–oxygen inert surface coating can also be constructed to avoid the formation of H_2S .^[26,27] Meanwhile, significant advancements have been made in the investigation of preventing the growth of lithium dendrites. Overall, strategies for inhibiting lithium dendrites can be divided into three broad categories: modification of the electrolyte itself (bulk phase doping,^[28,29] surface coating,^[30,31] electrolyte hybrid composite^[32,33]), introduction of interlayers,^[34,35] and optimization of lithium anode design (lithium surface engineering^[36–38] or substitution of lithium anode^[39–41]). Up to now, a considerable amount of literature related to the surface coating engineering have been published to significantly improve the air stability of sulfide SEs or the interface

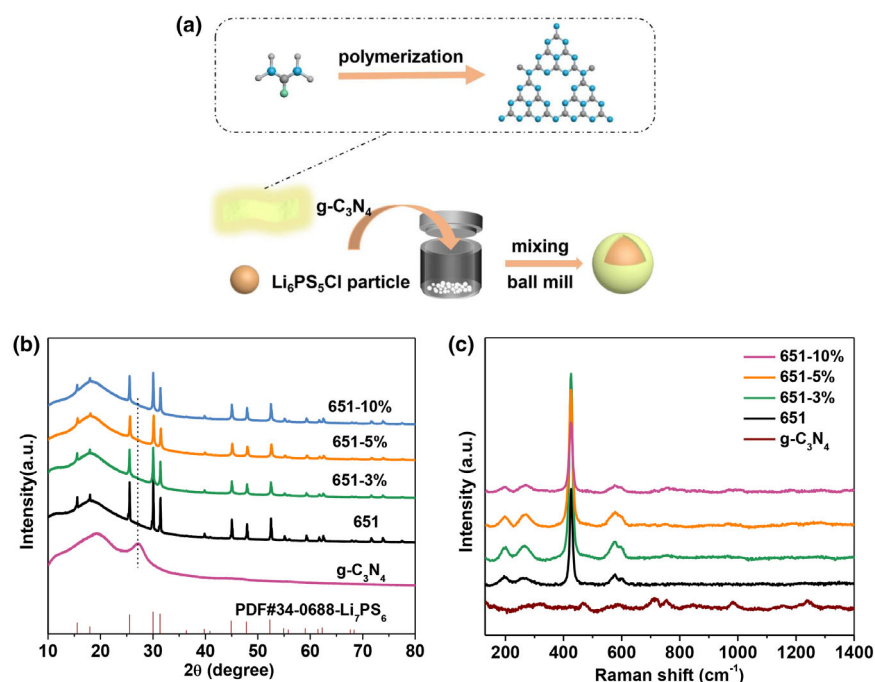


Figure 1. a) Schematic diagram of g-C₃N₄ and 651-x% solid electrolytes preparation. b) X-ray diffraction (XRD). And c) Raman spectra of g-C₃N₄ and 651-x% solid electrolytes.

stability of Li/sulfide SEs. However, the production of H₂S is not fundamentally inhibited.^[42–44] Hence, a promising surface coating strategy that can simultaneously significantly decrease the generation of H₂S and suppress dendrite formation remains lacking. g-C₃N₄, as a 2D polymer semiconductor material with a low electronic conductivity, is commonly used to prevent the formation of lithium dendrites for lithium metal batteries.^[45–47] Despite this, the application of g-C₃N₄ in sulfide solid-state lithium batteries is a topic seldom explored.

In this work, we coat a representative sulfide SE (Li₆PS₅Cl) with a thin layer of g-C₃N₄, which not only suppress lithium dendrite formation but also improve the air stability of sulfide SEs. By coating different proportions of g-C₃N₄ (0, 3, 5, and 10 wt%) on the surface of Li₆PS₅Cl particles through ball milling, it is found that g-C₃N₄ with an optimized amount of 5% can effectively lower the electronic conductivity of Li₆PS₅Cl and facilitate the in situ formation of ion-conductive Li₃N at the Li/Li₆PS₅Cl interface upon electrochemical cycling, thus effectively inhibiting lithium dendrite formation. Additionally, g-C₃N₄ coating on the surface enhances the humid air stability of Li₆PS₅Cl. As a result, the ASSLMs with 651-5% are able to attain a stable long cycle and high-capacity retention rate. The Li–Li symmetric battery with 651-5% exhibits minimal overpotential after cycles of 1000 h at 0.2 mA cm⁻². This effective and concise method holds significant implications for the progress of ASSLMs with enhanced safety and durability.

2. Results and Discussion

Figure 1a presents the schematic diagram of g-C₃N₄ and 651-x% preparation process. The layer g-C₃N₄ was obtained by calcining urea in a muffle furnace under ambient air at 550 °C. Different proportions of g-C₃N₄ and Li₆PS₅Cl were mixed by ball milling to obtain

g-C₃N₄-coated Li₆PS₅Cl (651-x%). As shown in **Figure 1b**, the XRD patterns show that the peaks at ~13° and ~27° correspond to the (100) and (002) crystal faces of g-C₃N₄, representing the in-plane ordering of the triazine ring and the tight stacking of the aromatic system between the planes, respectively. These results demonstrate the successful preparation of g-C₃N₄.^[48] Li₆PS₅Cl was successfully prepared with a cubic argyrodite-type structure, and its peak position agrees well with the known JCPDS card (34–0688).^[48] The XRD patterns for 651-3%, 651-5%, and 651-10% exhibited weak peaks at around 27°, but no visible hybrid peaks, which indicates the successful coating of g-C₃N₄ on Li₆PS₅Cl surface without side reactions. This conclusion is further corroborated by Raman spectra analysis. The peaks located at 469, 715, 755, and 982 cm⁻¹ denote the breathing pattern of the triazine ring, and the peak at 1238 cm⁻¹ represents the bending mode of –NH₂, which validates the successful preparation of g-C₃N₄.^[49,50] The five characteristic peaks of Li₆PS₅Cl at 196, 265, 425, 577, and 600 cm⁻¹ represent the vibration mode of PS₄³⁻, which verifies successful preparation of Li₆PS₅Cl with a cubic argyrodite-type structure.^[51] Compared

to Li₆PS₅Cl, the 651-x% (x = 3, 5, 10) exhibited no impurity peaks, suggesting excellent chemical stability between g-C₃N₄ and Li₆PS₅Cl. No discernible peak characteristic of g-C₃N₄ was observed in the 651-x% (x = 3, 5, 10). It is assumed that the strength of the Li₆PS₅Cl peak is considerable so that the characteristic peak of g-C₃N₄ is imperceptible. Overall, the XRD and Raman analyses prove the successful synthesis of g-C₃N₄ and Li₆PS₅Cl, and their excellent chemical compatibility.

Furthermore, scanning electron microscopy (SEM) and high-resolution transmission electron microscopy (HRTEM) were used to analyze the microscopic morphology of these materials. As shown in **Figure S1a**, Supporting Information, the average particle size of Li₆PS₅Cl was approximately 500 nm when 651-x% was pressed into electrolyte sheets. With the introduction of g-C₃N₄ (**Figure S1b–d**, Supporting Information), the morphology of 651-x% (x = 3, 5, 10) particles underwent significant changes. The g-C₃N₄ filled in the particle gap was distinctly visible. As illustrated in the HRTEM image of 651-5% (**Figure 2a**), the crystal face spacing of 0.269 nm corresponds to the (222) crystal face of Li₆PS₅Cl, aligning with the XRD and Raman analysis outcomes, demonstrating the successful synthesis of Li₆PS₅Cl. Moreover, **Figure 2a** exhibits a uniform amorphous coating layer (approximately 5 nm) on the outer surface of Li₆PS₅Cl particles, further confirmed by the HAADF-STEM and EDS spectra (**Figure 2b–g**). Overall, 5% g-C₃N₄ is coated on the surface of Li₆PS₅Cl particles, simultaneously filling the space between the particles.

The ionic conductivity measurement results were calculated based on the impedance spectra of cells with 651-x% solid electrolytes at 25 °C (**Figure S2**, Supporting Information) using Formula 1.1. As illustrated in **Figure 2h**, the ionic conductivity of 651-x% electrolytes gradually decreased (from 1.82 × 10⁻³ to 0.28 × 10⁻³ S cm⁻¹) with increasing g-C₃N₄ coating, attributed to the insufficient ionic conductivity of the g-C₃N₄. Furthermore, the activation energy is determined

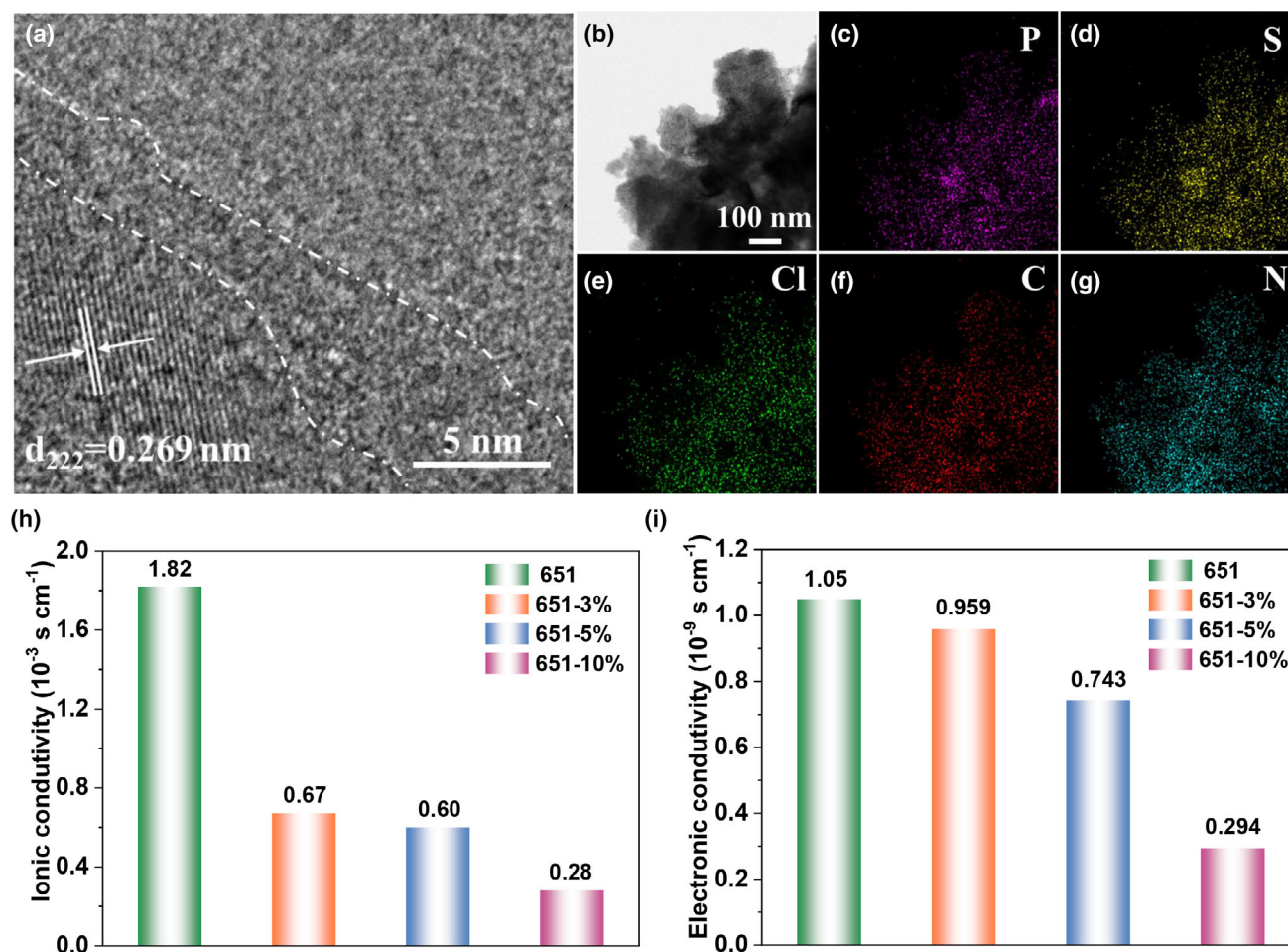


Figure 2. a) HRTEM, b) HAADF-STEM, and c–g) energy dispersive spectroscopy (EDS) of 651-5% solid electrolyte. h) Ionic conductivities and i) electronic conductivities of 651-x% solid electrolytes.

from the slope of Arrhenius plots of the cells with 651-x% solid electrolytes at different temperatures (Figure S3a, Supporting Information) using Formula 1.2. It is noteworthy that the activation energy reached its minimum (0.39 eV) when the g-C₃N₄ coating amount was 5% (Figure S3b, Supporting Information). Additionally, the electronic conductivity measurement data were obtained based on the current–time curves of 651-x% (Figure S4a–d, Supporting Information) using Formula 1.3. As a result, the electronic conductivity of 651-x% electrolytes gradually decreased from 1.05×10^{-9} to 0.29×10^{-9} S cm⁻¹ (Figure 2i). The decrease may be attributed to the low electronic conductivity of g-C₃N₄. These analyses suggest that Li₆PS₅Cl coated with 5% g-C₃N₄ facilitates favorable Li⁺ transfer and electron insulation, while also exhibiting a low activation energy.

In practical terms, the humid instability of Li₆PS₅Cl restricts its application in ASSLMBs. To investigate the effect of g-C₃N₄ coating on the air stability of the electrolytes, an air stability experiment was conducted with 651 and 651-5%. XPS spectra of 651 and 651-5% before and after air exposure are presented in Figure 3 and Figure S5, Supporting Information. In the P2p spectrum of 651 (Figure 3a), it is evident that P–O bonds (at 132.9 and 133.9 eV) formed due to the hydrolysis reaction of PS₄³⁻ when exposed to humid air.^[51] Sulfates (168.8 eV) and sulfites (166.9 eV) present in the S2p spectrum

(Figure S5a, Supporting Information) validate the oxidation of 651.^[52] The XPS spectra of 651-5% showed almost no by-product peaks in the P2p and S2p spectra after exposure, unlike those of 651 (Figure 3b and Figure S5b, Supporting Information). Furthermore, XRD spectra of 651 and 651-5% before and after exposure to air are shown in Figure 3c. For 651, the peak intensity of PO_xS_y, sulfate, and sulfite increased significantly after exposure for 3 h. Conversely, there was no significant change observed in the peak intensity of 651-5% after exposure to air. The aforementioned XPS and XRD analyses suggest that a 5% g-C₃N₄ coating can decrease the formation of by-products when 651-5% is exposed to humid air. Additionally, as shown in Figure 3d, the ionic conductivity was calculated based on the impedance spectra of 651 and 651-5% solid electrolytes before and after air exposure (Figure S6, Supporting Information). After exposure, the ionic conductivity (25 °C) of 651 after exposure decreased from 1.82 to 0.95 mS cm⁻¹, resulting in an ionic conductivity retention of 52%. In contrast, the ionic conductivity of 651-5% decreased from 0.6 to 0.45 mS cm⁻¹, resulting in an ionic conductivity retention of 72%. This indicates that the addition of 5 wt% g-C₃N₄ can effectively retard the decline in ionic conductivity. Overall, it is evident that 5% g-C₃N₄ coating on Li₆PS₅Cl can considerably enhance its humidity stability while maintaining satisfactory ionic conductivity.

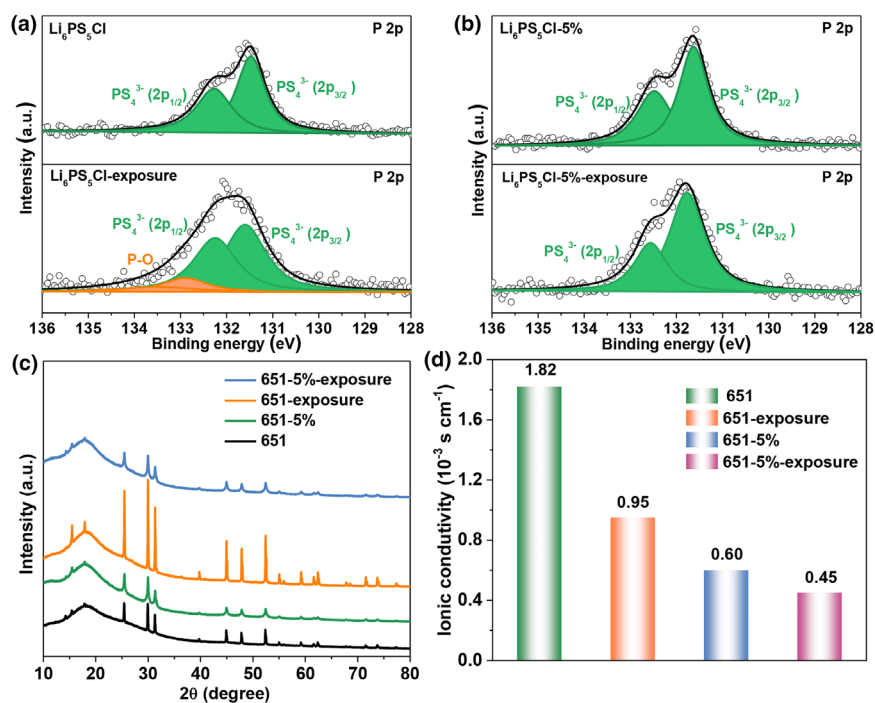


Figure 3. a, b) P2p X-ray Photoelectron Spectroscopy (XPS) spectra, c) XRD, d) Ionic conductivity of 651 and 651-5% solid electrolytes before and after air exposure.

To investigate the impact of $\text{g-C}_3\text{N}_4$ coating on lithium dendrite formation, the cycle performance of the Li–Li symmetric batteries with 651-x% was conducted at 0.2 mA cm^{-2} and 0.2 mAh cm^{-2} (Figure 4). The voltage polarization of the Li–Li symmetric battery with 651-5% cycling for 1000 h was remarkably smaller, measuring only 17 mV (Figure 4c). It is noteworthy that this cycle performance is superior to many reported studies on lithium/sulfide SEs interface modification (Table S1, Supporting Information). These results indicate much-improved stability at the interface between 651-5% and lithium metal. This stability may be attributed to the formation of an interphase with high ionic conductivity resulting from the reaction between the 651-5% electrolyte and lithium metal. Additionally, the low ionic conductivity of $\text{g-C}_3\text{N}_4$ on particle surfaces and interparticle impedes the flow of electron into the electrolyte, effectively preventing the growth of lithium dendrites into the electrolyte. In contrast, the symmetric battery with 651 experienced a short circuit for approximately 100 h. The voltage polarization of batteries with 651-3% and 651-10% reached 49 mV (after 1000 h) and 50 mV (after 850 h), respectively. The high-voltage polarization of the symmetric battery with 651 and 651-3% is attributed to the generation of by-product with low ionic conductivity and an increase in interface impedance. However, the excessive coating of $\text{g-C}_3\text{N}_4$ also results in poor ionic conductivity and increased polarization for the symmetric battery with 651-10%. This suggests that a 5% $\text{g-C}_3\text{N}_4$ coating enhances the cycle performance of the Li–Li symmetric battery with 651-5%.

To further investigate the inhibition effect of $\text{g-C}_3\text{N}_4$ coating on lithium dendrite formation, we conducted critical current density (CCD) tests on Li–Li symmetric cells with 651 and 651-5%. As shown in Figure S7a, Supporting Information, the Li–Li symmetrical battery with 651 experienced a short circuit at a current density of 0.5 mA cm^{-2} , resulting in a CCD of 0.4 mA cm^{-2} . In contrast, the Li–Li symmetrical

battery with 651-5% exhibited a CCD of 1 mA cm^{-2} , and a short circuit occurred when the current density reached 1.5 mA cm^{-2} (Figure S7b, Supporting Information). Compared to other reported studies on lithium/sulfide SEs' interface modification, the superior CCD and areal capacity value are shown in Table S2, Supporting Information. The enhanced CCD of the Li–Li symmetrical battery with 651-5% may be attributed to forming an interphase with high ionic conductivity between 651-5% and lithium metal. This interphase promotes uniform deposition of lithium and homogenizes the flow of Li^+ . Additionally, the $\text{g-C}_3\text{N}_4$ coating, with lower electronic conductivity, hinders the movement of electrons into the electrolyte phase. It is speculated that these factors collectively inhibit the growth of lithium dendrites.

To comprehend the inhibition capacity of $\text{g-C}_3\text{N}_4$ coating on lithium dendrites at elevated areal capacity of 0.5 mAh cm^{-2} , we examined the rate performance of the Li–Li symmetrical battery with 651 and 651-5% at 0.1, 0.25, and 0.5 mA cm^{-2} (Figure S8, Supporting Information). The Li–Li symmetrical battery with 651 displayed a sudden drop in overpotential when the current density reached 0.25 mA cm^{-2} ,

implying the occurrence of a noticeable short circuit. In comparison, the overpotential of the Li–Li symmetrical battery with 651-5% was only approximately 100 mV after 50 cycles at 0.5 mA cm^{-2} . Thus, the $\text{g-C}_3\text{N}_4$ coating can effectively inhibit the growth of lithium dendrites even with increased areal capacity, possibly due to the reaction of $\text{g-C}_3\text{N}_4$ with the Li anode to form Li_3N with high ionic conductivity, homogenizing lithium deposition. Additionally, $\text{g-C}_3\text{N}_4$, with insufficient electronic conductivity, can impede electron transfer to the electrolyte phase and alleviate the formation of dendrites.

ASSLMBs with 651-x% electrolytes were assembled to evaluate the influence of $\text{g-C}_3\text{N}_4$ coating on electrochemical performance. Figure 4e illustrates the cycling performance of ASSLMBs with 651-x% electrolytes at 0.1 C. As displayed in Figure S9, Supporting Information, the discharge capacity of ASSLMBs for the initial cycle at 0.1 C was 142.1, 137.4, 134.0, and 132.0 mAh g^{-1} , respectively. The corresponding coulombic efficiency was as follows: 82.49%, 81.54%, 81.32%, and 80.65%. Notably, ASSLMBs with 651-5% exhibited a discharge capacity of 5 mAh g^{-1} lower than that of ASSLMBs with 651. This may be attributed to the presence of $\text{g-C}_3\text{N}_4$, which reduces the ionic conductivity and hinders the electrochemical reaction kinetics. This is evidenced by the charge transfer impedance (R_{ct}) of ASSLMBs with 651 and 651-5% (285.97 and 316.3Ω) (Figure S10, Supporting Information). After 200 cycles, the discharge capacity was 26.9, 71.4, 132.8, and 47.5 mAh g^{-1} , and the retention rate was 18.9%, 51.9%, 99.1%, and 36%, respectively. The outstanding cycle performance of ASSLMBs with 651-5% outperforms the most reported studies listed in Table S3, Supporting Information. These results suggest that the $\text{g-C}_3\text{N}_4$ coating of 5% can effectively hinder the growth of lithium dendrites and enhance the cycle performance of ASSLMBs.

To further investigate the impact of $\text{g-C}_3\text{N}_4$ coating on lithium dendrites and interface stability, the cycle rate and areal loading of ASSLMBs

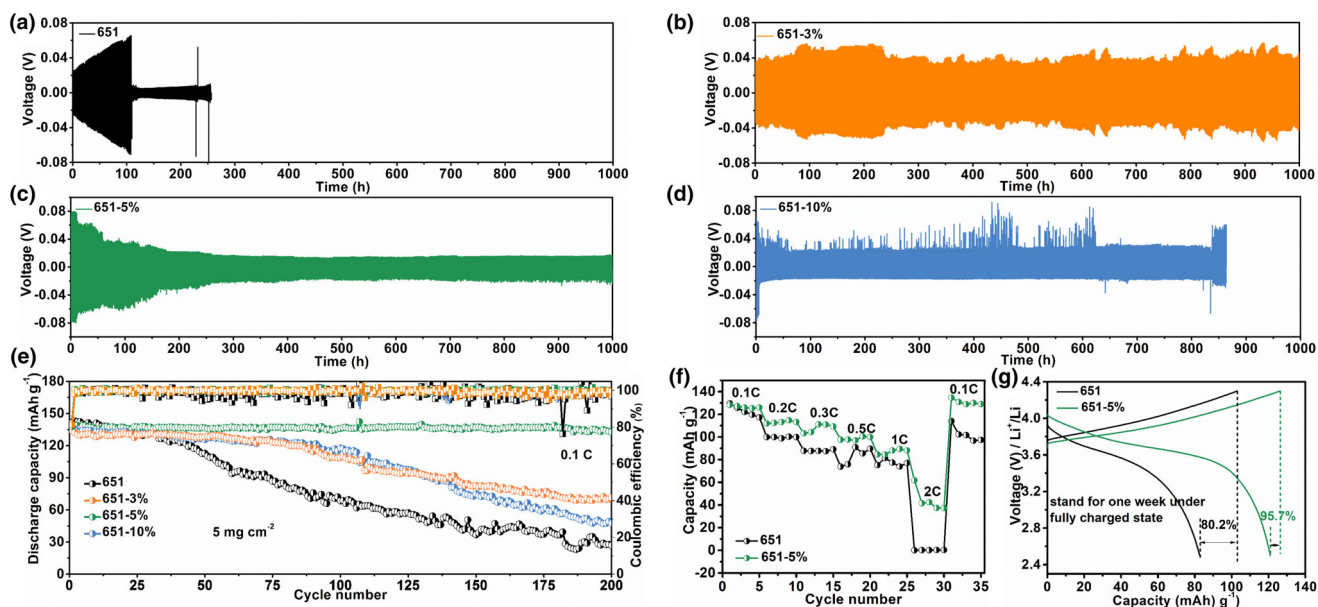


Figure 4. a–d) Cycle performance of Li–Li symmetric cells with 651-*x*% solid electrolytes at 0.2 mA cm⁻². e) Cycle performance of ASLMBs with 651-*x*% solid electrolytes at 0.1 C. f) Rate performance of ASLMBs with 651 and 651-5% solid electrolytes. g) Charge and discharge curves of ASLMBs with 651 and 651-5% solid electrolytes after standing for a week under fully charged state.

with 651-5% were increased. As the current density increased to 0.5 C (Figure S11b, Supporting Information), it can be seen that the ASLMBs with 651 and 651-5% exhibited the discharge capacities of 96.29, 96.08, and 113.57, 97.1 mAh g⁻¹, respectively, for the first and second cycles at 0.5 C (Figure S12, Supporting Information). The corresponding coulombic efficiency was 70.7%, 96.2%, and 75.89%, 98.8%, respectively. A short circuit was observed for the ASLMBs with 651 for only 5 cycles, causing a decrease in coulombic efficiency (from 96.2% to 25.1%). The extended charging process further confirms the occurrence of a short circuit. However, the ASLMBs with 651-5% still exhibited a discharge capacity of 64 mAh g⁻¹ after 64 cycles, and a capacity retention rate of approximately 66%. The findings suggest that even at 0.5 C, 651-5% continues to demonstrate a strong inhibitory effect on lithium dendrites. As illustrated in Figure S13, the Supporting Information, under the increased loading of cathode active materials, the cycle performance of the ASLMBs with 651 and 651-5% also affirms the aforementioned conclusions. The discharge capacity during the initial cycle at 0.05 C was 103.8 and 109.4 mAh g⁻¹, and the corresponding coulombic efficiency was 71.5% and 74.4%, respectively (Figure S14, Supporting Information). The capacity retention rate of the ASLMBs with 651 for 33 cycles was 20.5%, whereas that with 651-5% for 100 cycles was 59.7%. This further manifests that the 5% g-C₃N₄ coating can efficiently restrain lithium dendrite growth.

The rate performance test of the ASLMBs with 651 and 651-5% was also carried out to verify the inhibition of g-C₃N₄ on lithium dendrites. As illustrated in Figure 4f, the discharge capacity of the ASLMBs with 651-5% at various rates was higher compared to those with 651, indicating improved rate performance. When the rate was as high as 2 C, basically no capacity was released for the battery with 651, while the battery with 651-5% still achieved a discharge capacity of 61.8 mAh g⁻¹. In addition, upon the rates reverting back to 0.1 C, the discharge capacity of the ASLMBs with 651 was 114 mAh g⁻¹, while those with the 651-5% rose to 134.7 mAh g⁻¹. Evidently, as the rate

increased to 1 C, the charging curve of ASLMBs with 651 depicted abnormal behavior (Figure S15a, Supporting Information), indicating micro-short circuit due to dendrite growth. Moreover, no capacity was released at 2 C. In contrast, the charge and discharge curve of the ASLMBs with the 651-5% was normal (Figure S15b, Supporting Information), signifying that 5% g-C₃N₄ coating can efficiently inhibit the growth of dendrites.

To assess the impact of g-C₃N₄ coating on the self-discharge behavior of the batteries, the ASLMBs with 651 and 651-5% underwent a self-discharge experiment. As shown in Figure 4g, the batteries reached a stable state after 3 cycles at 0.1 C, with corresponding coulombic efficiency of 98.4% and 99.6%, respectively. After being fully charged to 4.3 V, the battery was left to stand for 168 hours before being discharged to 2.5 V. The coulombic efficiency of ASLMBs with 651 decreased by 18.2% (80.2%), and the self-discharge behavior was severe due to the non-negligible electronic conductivity of 651. In contrast, ASLMBs with 651-5% exhibited a mere 3.9% reduction (95.7%) in coulombic efficiency, nearly five times lower than the self-discharge rate of ASLMBs with 651. The voltage curve (Figure S16, Supporting Information) indicates that ASLMBs with 651-5% experience slower voltage drops, suggesting that the g-C₃N₄ coating can reduce the electronic conductivity of 651-5%, thereby improving self-discharge behavior.

To examine the interface reaction and evolution of Li–Li symmetric batteries with 651 and 651-5% electrolytes at various cycles (0, 1, 2, 10, 30, 50, and 100 cycles), in situ Electrochemical Impedance Spectroscopy (EIS) measurement of the batteries was conducted on the batteries (Figure 5a,d), and the resultant data were analyzed using DRT.^[53] Based on the DRT results (Figure 5b,c), the peak areas of τ_1 (about 10⁻⁶ s) and τ_3 (1–10 s) for the Li–Li symmetric battery with 651 initially increased significantly with cycling. This suggests that an interface reaction occurred between Li metal and 651 during cycling, leading to the generation of an interfacial layer with a low ionic conductivity.^[54] Consequently, the interface impedance increased. The

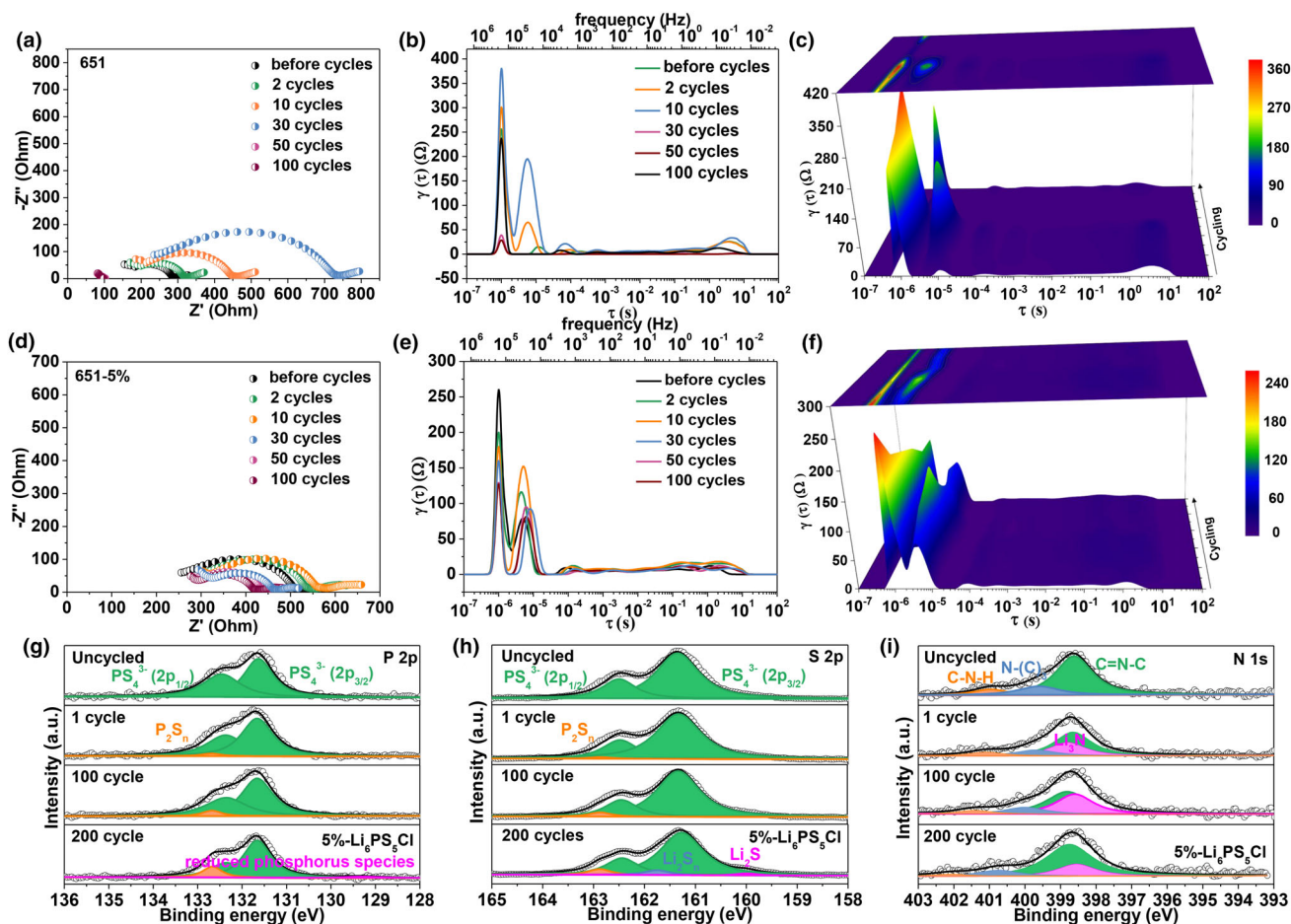


Figure 5. Impedance spectra and the corresponding distribution of relaxation times (DRT) transformation of the Li-Li symmetric batteries with a–c) 651 and d–f) 651-5% solid electrolytes at various cycles. g) P 2p, h) S 2p, and i) N 1s XPS spectra of the Li-Li symmetric batteries with 651-5% solid electrolyte at various cycles.

peak area sharply decreased when the Li–Li symmetrical battery with 651 was cycled for 50 and 100 cycles, indicating the occurrence of a short circuit. However, for the Li–Li symmetric battery with 651-5% (Figure 5e,f), the peak area of τ_1 (about 10^{-6} s), τ_2 (10^{-1} s), and τ_3 (1–10 s) exhibited a gradual decrease as the cycle number increased. This observation indicates a decline in interface impedance, which can be attributed to the generation of the Li_3N interface layer resulting from the reaction of Li metal and the $\text{g-C}_3\text{N}_4$. The DRT analysis results indicate that the in situ Li_3N intermediate layer leads to relatively uniform Li^+ flow, efficiently restraining the formation of lithium dendrites.^[45]

To examine the interface composition of the battery interface during cycling, the electrolytes obtained from Li–Li symmetric batteries with various cycles were subjected to XPS analysis. For XPS spectra of 651 electrolyte for Li–Li symmetrical battery at different cycles (Figure S17, Supporting Information), it is observed that the peak area of PS_4^{2-} , intrinsic to the 651 electrolyte, gradually decreased with the progression of the cycle. Simultaneously, the peak area of decomposition by-product P_2S_n increased gradually, and the interface reaction by-product such as Li_2S_n , Li_2S , and reduced phosphorous products also showed a gradual increase. This indicates that the decomposition and interface reactions continue to occur during the cycles. In contrast, for Li–Li symmetric batteries with 651-5%, XPS

analyses of S, P, and N elements of 651-5% at different cycles are presented in Figure 5g–i. The peak area of PS_4^{2-} , inherent in 651-5% solid electrolyte, decreased gradually. In addition, the peak area of decomposition by-product P_2S_n increased gradually but less than that of 651 electrolytes. This finding indicates that the $\text{g-C}_3\text{N}_4$ coating can effectively inhibit the decomposition reaction of 651 electrolyte. Moreover, the by-products of interfacial reactions, such as Li_2S_n , Li_2S , and reduced phosphate-containing products, were observed only when the cycle surpassed 200, indicating that the coating of $\text{g-C}_3\text{N}_4$ exerts some inhibitory effect on the reaction between the lithium and $\text{Li}_6\text{PS}_5\text{Cl}$. Furthermore, the peak area of Li_3N in N 1s spectra increased gradually, indicating that $\text{g-C}_3\text{N}_4$ and Li anode continue to react and produce Li_3N with high ionic conductivity upon cycling. This enables the uniform deposition of Li and effectively inhibits lithium dendrite formation.

To further verify the impact of $\text{g-C}_3\text{N}_4$ coating on the post-cycle interface of Li–Li symmetric batteries, Raman tests of the electrolyte interface obtained from the post-cycle Li–Li symmetric batteries were conducted. Raman spectra of the electrolyte interface of the Li–Li symmetric battery with 651 after cycling (Figure S18, Supporting Information) displayed a fresh peak of Li_2S (379.7 cm^{-1}) alongside the typical 651 peak. In contrast, for the Li–Li symmetric battery with 651-5%, a

new Li_3N peak at about 600 cm^{-1} appeared with no detectable Li_2S peak. This indicates that the presence of $\text{g-C}_3\text{N}_4$ can well suppress the side reaction between 651 and lithium metal. Moreover, the presence of Li_3N with high ionic conductivity further supports the XPS analysis results discussed above.

SEM and EDS tests were further conducted to determine the elemental distribution across the cross-section of the electrolytes sheet in Li–Li symmetric batteries with 651 and 651-5% after cycling. The presence of Li dendrites in the electrolyte phase can be deduced from the uneven distribution of S, P, and Cl elements in the EDS image of the 651 electrolyte sheets post-cycles (Figure S19, Supporting Information). This is attributed to the high electronic conductivity of 651, leading to the reduction of Li^+ by electrons entering the electrolyte phase. In the Li–Li symmetrical battery with 651-5%, the distribution of elements (S, P, Cl, C, and N) in the 651-5% electrolyte sheets remained uniform even after 200 cycles. It can be inferred that the presence of $\text{g-C}_3\text{N}_4$ coating effectively hinders the electron transfer to the 651-5% electrolyte phase, thereby inhibiting the growth of Li dendrites in the electrolyte.

Density functional theory (DFT) theoretical calculation, including electrostatic potential and PDOS, were further employed to explain the mechanism of lithium dendrites inhibition using $\text{g-C}_3\text{N}_4$ coating. Optimal configuration diagram of different interfaces ($\text{Li-Li}_6\text{PS}_5\text{Cl}$, $\text{Li-g-C}_3\text{N}_4$, and $\text{Li}_6\text{PS}_5\text{Cl-g-C}_3\text{N}_4$) is displayed in Figure S21, Supporting Information. After being unified into a heterojunction interface model, the three interfaces exhibited good stability after optimization, with no observable chaos or reconstruction. Figure 6a–c displays the calculated electrostatic potential of the three interfaces with corresponding values of 3.23, 3.68, and 4.38 eV, respectively. Significant barriers existed for electrons flowing from Li to $\text{g-C}_3\text{N}_4$ or from $\text{Li}_6\text{PS}_5\text{Cl}$ to $\text{g-C}_3\text{N}_4$, both exceeding the barriers for electrons flowing from Li to $\text{Li}_6\text{PS}_5\text{Cl}$. This suggests that Li^+ can easily penetrate the bulk phase of $\text{Li}_6\text{PS}_5\text{Cl}$, where reduction occurs, rather than at the interface. The electrostatic potential (3.68 eV) between Li and $\text{g-C}_3\text{N}_4$ implies an energy barrier that must be overcome (3.68 eV) when electrons are transferred into the $\text{Li-g-C}_3\text{N}_4$ interface. This suggests that $\text{g-C}_3\text{N}_4$ coating may hinder the permeation of lithium dendrites into the electrolyte. Additionally,

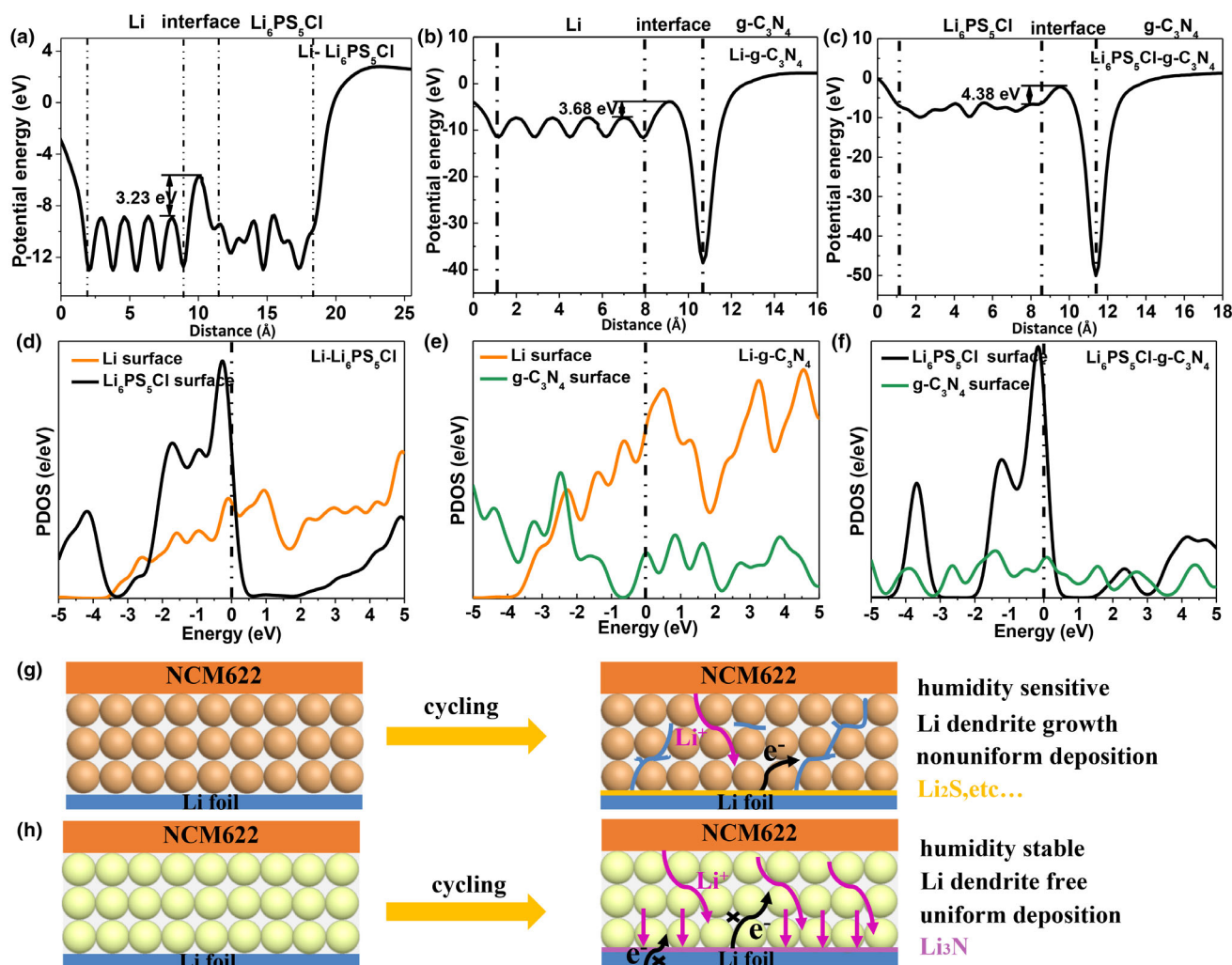


Figure 6. The electrostatic potential profiles of a) Li (100)/ $\text{Li}_6\text{PS}_5\text{Cl}$ (100), b) Li (100)/ $\text{g-C}_3\text{N}_4$, and c) $\text{Li}_6\text{PS}_5\text{Cl}$ (100)/ $\text{g-C}_3\text{N}_4$. The projected density of states (PDOS) of d) Li (100)/ $\text{Li}_6\text{PS}_5\text{Cl}$ (100), e) Li (100)/ $\text{g-C}_3\text{N}_4$, and f) $\text{Li}_6\text{PS}_5\text{Cl}$ (100)/ $\text{g-C}_3\text{N}_4$. The underlying mechanism diagram of the ASSLMBs with g) 651 and h) 651-5% solid electrolytes.

the electrostatic potential between $\text{Li}_6\text{PS}_5\text{Cl}$ and $\text{g-C}_3\text{N}_4$ was 4.38 eV, suggesting that $\text{g-C}_3\text{N}_4$ filling the gap in $\text{Li}_6\text{PS}_5\text{Cl}$ particles prevents electron flowing to the $\text{Li}_6\text{PS}_5\text{Cl}$ electrolyte phase, thereby inhibiting the growth of Li dendrites in the electrolyte. Figure 6d illustrates the highly conductive interface between Li and $\text{Li}_6\text{PS}_5\text{Cl}$, facilitating easy ingress of electrons into the interior of $\text{Li}_6\text{PS}_5\text{Cl}$. This leads to the growth of lithium dendrites in the electrolyte, as indicated by the PDOS calculation results. Remarkably, the electronic insulation property of $\text{g-C}_3\text{N}_4$ was demonstrated (Figure 6e,f). Based on the previous analysis, Figure 6g,h clearly illustrates the underlying mechanism. The in situ generated Li_3N intermediate layer in the battery with 651-5% electrolyte homogenizes Li^+ flow and facilitates the uniform deposition of Li. Additionally, the $\text{g-C}_3\text{N}_4$ coating with low electronic conductivity effectively prevents the transfer of electrons to the 651 electrolyte phase, inhibiting the growth of Li dendrites in the bulk phase, and enhancing the electrochemical performance of the batteries.

3. Conclusion

In this work, the layer $\text{g-C}_3\text{N}_4$ was prepared through a one-step calcination method in air, and the 651-x% ($x = 0, 3, 5, 10$) was successfully produced using a low-speed ball milling technique. The incorporation of a 5% $\text{g-C}_3\text{N}_4$ coating is strategically chosen to optimize Li^+ transfer and electron insulation, simultaneously minimizing by-product formation in humid conditions. The $\text{g-C}_3\text{N}_4$ with low electronic conductivity could impede the ingress of electrons into $\text{Li}_6\text{PS}_5\text{Cl}$, which aligns well with DFT calculation. Moreover, the in situ Li_3N intermediate layer facilitates a uniform flow of Li^+ , effectively mitigating the formation of lithium dendrites. As a consequence, the Li–Li symmetric battery with 651-5% can stably cycle for 1000 h, exhibiting reduced voltage polarization (17 mV). ASSLMs utilizing the 651-5% electrolyte demonstrate a notable capacity of 132.8 mAh g^{-1} after 200 cycles, with an impressive retention rate of 99.1%. This research contributes valuable insights into the coating modification of sulfide solid electrolytes, offering inspiration for the advancement of ASSLMs characterized by enhanced safety and prolonged cycle life.

4. Experimental Section

Synthesis of 651-x%: $\text{Li}_6\text{PS}_5\text{Cl}$ solid-state electrolyte was synthesized by China Automotive Battery Research Institute Co., Ltd. 10 g urea was placed into the crucible and subsequently calcined in the muffle furnace at 520 °C for 5 h, and then, the $\text{g-C}_3\text{N}_4$ nanosheets can be obtained. The $\text{g-C}_3\text{N}_4$ proportion in $\text{Li}_6\text{PS}_5\text{Cl}$ - $\text{g-C}_3\text{N}_4$ combination was regulated to 0, 3, 5, and 10 wt% (hereinafter referred to as 651-x%, $x = 0, 3, 5, 10$), and then, the blend was enclosed inside a zirconia ball mill jar in Ar atmosphere ball milling at 300 rpm for 12 h to prepare 651-x%.

Ionic conductivity and electronic conductivity measurements: The ionic conductivity of 651-x% was calculated by EIS test at various temperatures (5, 15, 25, 35, 45, and 55 °C). Solid electrolyte powders were positioned between two stainless steel cylinders of the mold and pressed into electrolyte sheets under a pressure of 300 MPa. Then, a suitable quantity of CNTs was applied to each side of the electrolyte sheets in order to enhance the connection interface. The EIS was tested on the Autolab electrochemical workstation at a frequency ranging from 1 Hz to 1 MHz and an amplitude of 10 mV. Formula 1.1 is utilized to compute the ionic conductivity (σ). R denotes the resistance value, L is the thickness of the electrolyte sheets, and S is the area of the electrolyte sheets. The activation energy (E_a) is calculated using the Formula 1.2, where σ denotes the ionic conductivity, A refers to the prefactor, T stands for the absolute temperature, and k_B represents the Boltzmann constant. Formula 1.3 is used to calculate the electronic conductivity (σ), with Δd representing the thickness of the electrolyte sheet, S

representing the area of the electrolyte sheet, U representing the polarization voltage, and I representing the steady-state current.

$$\sigma = \frac{L}{RS} \quad (1.1)$$

$$\sigma = \frac{A}{T} e^{-E_a/k_B T} \quad (1.2)$$

$$\sigma = \frac{\Delta d}{U/(I \cdot S)} \quad (1.3)$$

Stability measurements of 651 and 651-5% in humid air: The humid air stability of 651 and 651-5% was tested in a closed simple glove box with 20% relative humidity through placing equal masses of 651 and 651-5% powders in open vials for 3 hours. XRD, XPS, and EIS were used to characterize the stability of 651 and 651-5% powders in humid air.

Material characterization: XRD patterns were conducted using a Br SmartLab Rigaku instrument equipped with a Cu K α radiation. The morphology of the 651 and 651-5% electrolyte sheets before and after cycles was examined by SEM (Hitachi S-4800) with EDS. XPS was performed using Krotos AXIS Ultra Spectrometer. The spatial distribution of $\text{g-C}_3\text{N}_4$ in 651-5% and the crystal structure of the 651 and 651-5% were characterized through cryo-TEM (Talos F200X G2) equipped with EDS.

DFT calculations: The computations were carried out utilizing the first-principles calculation implementation of CASTEP.^[55] To account for exchange-correlation potential, the generalized gradient approximation (GGA)^[56] with the Perdew–Burke–Ernzerhof (PBE) formula^[57] in conjunction with the DFT-D correction was employed. The Broyden–Fletcher–Goldfarb–Shanno (BFGS) method was used to identify the ground state of the supercells. The convergence tolerance was set to the energy change below 10^{-5} eV per atom, force less than 0.02 eV \AA^{-1} , stress less than 0.05 GPa, and displacement change less than 0.001 \AA . The cutoff energy of the atomic wave functions was designated as 450 eV.

Assembly and electrochemical measurements of Li–Li symmetrical batteries: First, 100 mg of 651-x% powders was placed in a PTFE mold and subjected to a pressure of ~300 MPa to form an electrolyte sheet. Then, two lithium foils with a diameter of 10 mm and a thickness of 40 μm were placed on both sides of the electrolyte sheet with a pressure of 30 MPa. The deposition and stripping experiments of Li–Li symmetric cells were tested in the LAND battery test system at a current density of 0.2–2 mA cm^{-2} and an areal capacity of 0.2/0.5 mAh cm^{-2} . The specific battery test conditions were reflected in the main text.

Preparation of cathode: $\text{LiNi}_{0.6}\text{Mn}_{0.2}\text{Co}_{0.2}\text{O}_2$ coated with LiNbO_3 (NCM622) (LNO@NCM) was synthesized by China Automotive Battery Research Institute Co., Ltd. The LNO@NCM Powder and $\text{Li}_6\text{PS}_5\text{Cl}$ were milled using a mass ratio of 7:3, and a rotation speed of 200 rpm for 6 h, without adding conductive carbon.

Assembly and electrochemical measurements of the ASSLMs: The assembly of ASSLMs was operated within an Ar-filled glove box. 100 mg of 651-x% powders was placed between two stainless steel cylinders s in a mold under pressure of 240 MPa and pressed into electrolyte sheets. The lithium foil was inserted on one side of the electrolyte layer under a pressure of 30 MPa. The mass loading of the LNO@NCM cathode materials was 5 and 10.5 mg cm^{-2} , respectively. The test of the ASSLMs was conducted using the LAND battery test system at varying rate (0.1–2 C) and the voltage ranging from 2.5–4.3 V, and the specific battery test conditions were detailed in the main text.

Self-discharge measurements: The ASSLMs underwent an initial cycling at 0.1 C for 3 cycles. Subsequently, it was charged to 4.3 V and left to stand for a week, specifically 168 h. Following this, the battery was discharged to 2.5 V. The calculated capacity retention rate was then used to evaluate the self-discharge behavior of the battery.

Acknowledgements

This work was supported by Beijing Natural Science Foundation (JQ22028), National Natural Science Foundation of China (U21A2080), Jilin Province Science and Technology Major Project (20210301021GX), and Ministry of Science and Technology Rare Earth Special (2022YFB3506300).

Conflict of Interest

There authors declare no conflict of interest.

Supporting Information

Supporting Information is available from the Wiley Online Library or from the author.

Keywords

anode interface, g-C₃N₄ coating, Li₆PS₅Cl, lithium dendrite inhibition, solid-state lithium metal batteries

Received: December 4, 2023
Revised: December 27, 2023
Published online: January 7, 2024

- [1] Z. P. Cano, D. Banham, S. Ye, A. Hintennach, J. Lu, M. Fowler, Z. Chen, *Nat. Energy* **2018**, 3, 279.
- [2] J. B. Goodenough, K. S. Park, *J. Am. Chem. Soc.* **2013**, 135, 1167.
- [3] J. M. Tarascon, M. Armand, *Nature* **2001**, 414, 359.
- [4] J. Deng, C. Bae, A. Denlinger, T. Miller, *Joule* **2020**, 4, 511.
- [5] Z. Zhang, J. Wang, S. Zhang, H. Ying, Z. Zhuang, F. Ma, P. Huang, T. Yang, G. Han, W. Q. Han, *Energy Storage Mater.* **2021**, 43, 229.
- [6] X. Ke, Y. Wang, L. Dai, C. Yuan, *Energy Storage Mater.* **2020**, 33, 309.
- [7] Z. Liang, Y. Xiang, K. Wang, J. Zhu, Y. Jin, H. Wang, B. Zheng, Z. Chen, M. Tao, X. Liu, *Nat. Commun.* **2023**, 14, 259.
- [8] Z. Wu, Z. Xie, A. Yoshida, Z. Wang, X. Hao, A. Abudula, G. Guan, *Renew. Sustain. Energy Rev.* **2019**, 109, 367.
- [9] X. Chen, Z. Guan, F. Chu, Z. Xue, F. Wu, Y. Yu, *InfoMat* **2022**, 4, e12248.
- [10] T. Ma, Z. Wang, D. Wu, P. Lu, X. Zhu, M. Yang, J. Peng, L. Chen, H. Li, F. Wu, *Energ. Environ. Sci.* **2023**, 16, 2142.
- [11] P. Lu, Y. Xia, G. Sun, D. Wu, S. Wu, W. Yan, X. Zhu, J. Lu, Q. Niu, S. Shi, *Nat. Commun.* **2023**, 14, 4077.
- [12] W. Yan, Z. Mu, Z. Wang, Y. Huang, D. Wu, P. Lu, J. Lu, J. Xu, Y. Wu, T. Ma, *Nat. Energy* **2023**, 8, 800.
- [13] Y. Li, S. Song, H. Kim, K. Nomoto, H. Kim, X. Sun, S. Hori, K. Suzuki, N. Matsui, M. Hirayama, *Science* **2023**, 381, 50.
- [14] C. Wang, J. Liang, Y. Zhao, M. Zheng, X. Li, X. Sun, *Energ. Environ. Sci.* **2021**, 14, 2577.
- [15] L. Zhang, X. Zhang, Z. Rong, T. Wang, Z. Wang, Z. Wang, L. Zhang, Q. Huang, L. Zhu, L. Zhang, *Nano Res.* **2023**, 16, 10966.
- [16] J. Wu, S. Liu, F. Han, X. Yao, C. Wang, *Adv. Mater.* **2021**, 33, 2000751.
- [17] Q. Zhang, D. Cao, Y. Ma, A. Natan, P. Aurora, H. Zhu, *Adv. Mater.* **2019**, 31, 1901131.
- [18] Q. Yang, N. Deng, J. Chen, B. Cheng, W. Kang, *Chem. Eng. J.* **2021**, 413, 127427.
- [19] A. Hayashi, H. Muramatsu, T. Ohtomo, S. Hama, M. Tatsumisago, *J. Mater. Chem. A* **2013**, 1, 6320.
- [20] T. Ohtomo, A. Hayashi, M. Tatsumisago, K. Kawamoto, *J. Mater. Sci.* **2013**, 48, 4137.
- [21] D. Lee, K. H. Park, S. Y. Kim, J. Y. Jung, W. Lee, K. Kim, G. Jeong, J. S. Yu, J. Choi, M.-S. Park, *J. Mater. Chem. A* **2021**, 9, 17311.
- [22] Z. Zhang, L. Zhang, X. Yan, H. Wang, Y. Liu, C. Yu, X. Cao, L. van Eijck, B. Wen, *J. Power Sources* **2019**, 410, 162.
- [23] M. Xu, S. Song, S. Daikuhara, N. Matsui, S. Hori, K. Suzuki, M. Hirayama, S. Shiotani, S. Nakanishi, M. Yonemura, *Inorg. Chem.* **2021**, 61, 52.
- [24] L. Ye, E. Gil-González, X. Li, *Electrochem. Commun.* **2021**, 128, 107058.
- [25] F. Zhao, J. Liang, C. Yu, Q. Sun, X. Li, K. Adair, C. Wang, Y. Zhao, S. Zhang, W. Li, *Adv. Energy Mater.* **2020**, 10, 1903422.
- [26] W. D. Jung, M. Jeon, S. S. Shin, J. S. Kim, H. G. Jung, B. K. Kim, J. H. Lee, Y. C. Chung, H. Kim, *ACS Omega* **2020**, 5, 26015.
- [27] J. Xu, Y. Li, P. Lu, W. Yan, M. Yang, H. Li, L. Chen, F. Wu, *Adv. Energy Mater.* **2022**, 12, 2102348.
- [28] Z. Zhang, Y. Tian, G. Liu, M. Wu, H. He, X. Yao, *J. Electrochem. Soc.* **2022**, 169, 40553.
- [29] Z. Jiang, H. Peng, Y. Liu, Z. Li, Y. Zhong, X. Wang, X. Xia, C. Gu, J. Tu, *Adv. Energy Mater.* **2021**, 11, 2101521.
- [30] Y. Wang, J. Ju, S. Dong, Y. Yan, F. Jiang, L. Cui, Q. Wang, X. Han, G. Cui, *Adv. Funct. Mater.* **2021**, 31, 2101523.
- [31] J. Li, Y. Li, J. Cheng, Q. Sun, L. Dai, N. Ci, D. Li, L. Ci, *J. Power Sources* **2022**, 518, 230739.
- [32] L. Ye, X. Li, *Nature* **2021**, 593, 218.
- [33] X. Yao, N. Huang, F. Han, Q. Zhang, H. Wan, J. P. M. Wizerwa, C. Wang, X. Xu, *Adv. Energy Mater.* **2017**, 7, 1602923.
- [34] Y. Su, L. Ye, W. Fitzhugh, Y. Wang, E. Gil-González, I. Kim, X. Li, *Energ. Environ. Sci.* **2020**, 13, 908.
- [35] X. Ji, S. Hou, P. Wang, X. He, N. Piao, J. Chen, X. Fan, C. Wang, *Adv. Mater.* **2020**, 32, 2002741.
- [36] H. Park, J. Kim, D. Lee, J. Park, S. Jo, J. Kim, T. Song, U. Paik, *Adv. Sci.* **2021**, 8, 2004204.
- [37] C. Duan, Z. Cheng, W. Li, F. Li, H. Liu, J. Yang, G. Hou, P. He, H. Zhou, *Energ. Environ. Sci.* **2022**, 15, 3236.
- [38] C. Wang, X. Sun, L. Yang, D. Song, Y. Wu, T. Ohsaka, F. Matsumoto, J. Wu, *Adv. Mater. Interfaces* **2021**, 8, 2001698.
- [39] S. Luo, Z. Wang, X. Li, X. Liu, H. Wang, W. Ma, L. Zhang, L. Zhu, X. Zhang, *Nat. Commun.* **2021**, 12, 6968.
- [40] L. Yong Gun, F. Satoshi, J. Changhoon, N. Suzuki, Y. Nobuyoshi, O. Ryo, S. Tomoyuki, R. Saebom, J. H. Ku, W. Taku, *Nat. Energy* **2020**, 5, 299.
- [41] J. Asenbauer, T. Eisenmann, M. Kuenzel, A. Kazzazi, Z. Chen, D. Bresser, *Sustain. Energ. Fuels* **2020**, 4, 5387.
- [42] G. Liu, J. Shi, M. Zhu, W. Weng, L. Shen, J. Yang, X. Yao, *Energy Storage Mater.* **2021**, 38, 249.
- [43] W. Weng, D. Zhou, G. Liu, L. Shen, M. Li, X. Chang, X. Yao, *Mater. Futures* **2022**, 1, 21001.
- [44] Y. Jin, Q. He, G. Liu, Z. Gu, M. Wu, T. Sun, Z. Zhang, L. Huang, X. Yao, *Adv. Mater.* **2023**, 35, 2211047.
- [45] Y. Huang, B. Chen, J. Duan, F. Yang, T. Wang, Z. Wang, W. Yang, C. Hu, W. Luo, Y. Huang, *Angew. Chem. Int. Ed.* **2020**, 132, 3728.
- [46] Y. Guo, P. Niu, Y. Liu, Y. Ouyang, D. Li, T. Zhai, H. Li, Y. Cui, *Adv. Mater.* **2019**, 31, 1900342.
- [47] L. Chen, T. Gu, J. Ma, K. Yang, P. Shi, J. Biao, J. Mi, M. Liu, W. Lv, Y. B. He, *Nano Energy* **2022**, 100, 107470.
- [48] S. J. Liu, F. T. Li, Y. L. Li, Y. J. Hao, X. J. Wang, B. Li, R. H. Liu, *Appl. Catal. Environ.* **2017**, 212, 115.
- [49] P. Kumar, E. Vahidzadeh, U. K. Thakur, P. Kar, K. M. Alam, A. Goswami, N. Mahdi, K. Cui, G. M. Bernard, V. K. Michaelis, *J. Am. Chem. Soc.* **2019**, 141, 5415.
- [50] S. Tonda, S. Kumar, S. Kandula, V. Shanker, *J. Mater. Chem. A* **2014**, 2, 6772.
- [51] H. Xu, G. Cao, Y. Shen, Y. Yu, J. Hu, Z. Wang, G. Shao, *Energy Environ. Mater.* **2022**, 5, 852.
- [52] X. Yang, X. Gao, Q. Sun, S. P. Jand, Y. Yu, Y. Zhao, X. Li, K. Adair, L. Y. Kuo, J. Rohrer, *Adv. Mater.* **2019**, 31, 1901220.
- [53] H. Duan, C. Wang, R. Yu, W. Li, J. Fu, X. Yang, X. Lin, M. Zheng, X. Li, S. Deng, *Adv. Energy Mater.* **2023**, 13, 2300815.
- [54] Y. Lu, C. Z. Zhao, R. Zhang, H. Yuan, L. P. Hou, Z. H. Fu, X. Chen, J. Q. Huang, Q. Zhang, *Sci. Adv.* **2021**, 7, eabi5520.
- [55] V. Milman, B. Winkler, J. White, C. Pickard, M. Payne, E. Akhmatkaya, R. Nobes, *Int. J. Quantum Chem.* **2000**, 77, 895.
- [56] J. P. Perdew, A. Ruzsinszky, G. I. Csonka, O. A. Vydrov, G. E. Scuseria, L. A. Constantin, X. Zhou, K. Burke, *Phys. Rev. Lett.* **2008**, 100, 136406.
- [57] J. P. Perdew, K. Burke, M. Ernzerhof, *Phys. Rev. Lett.* **1996**, 77, 3865.